*J. Fluid Mech.* (1989), *vol.* 209, *pp.* 543–566
*Printed in Great Britain*



# Viscous and inviscid flows in a channel with a moving indentation

By M. E. RALPH† AND T. J. PEDLEY
Department of Applied Mathematics and Theoretical Physics, University of Cambridge, Silver Street, Cambridge CB3 9EW, UK

(Received 5 January 1988 and in revised form 3 July 1989)

The flow in a channel with an oscillating constriction has been studied by the numerical solution of the Navier–Stokes and Euler equations. A vorticity wave is found downstream of the constriction in both viscous and inviscid flow, whether the downstream flow rate is held constant and the upstream flow is pulsatile, or vice versa. Closed eddies are predicted to form between the crests/troughs of the wave and the walls, in the Euler solutions as well as the Navier–Stokes flows, although their structures are different in the two cases.

The positions of wave crests and troughs, as determined numerically, are compared with the predictions of a small-amplitude inviscid theory (Pedley & Stephanoff 1985). The theory agrees reasonably with the Euler equation predictions at small amplitude ($\epsilon \lesssim 0.2$) as long as the downstream flow rate is held fixed; otherwise a sinusoidal displacement is superimposed on the computed crest positions. At larger amplitude ($\epsilon = 0.38$) the wave crests move downstream more rapidly than predicted by the theory, because of the rapid growth of the first eddy ('eddy A') attached to the downstream end of the constriction. At such larger amplitudes the Navier–Stokes predictions also agree well with the Euler predictions, when the downstream flow rate is held fixed, because the wave generation process is essentially inviscid and the undisturbed vorticity distribution is the same in each case. It is quite different, however, when the upstream flow rate is fixed, as in the experiments of Pedley & Stephanoff, because of differences in the undisturbed vorticity distribution, in the growth rate of the vorticity waves and in the dynamics of eddy A. A further finite-amplitude effect of importance, especially in an inviscid fluid, is the interaction of an eddy with its images in the channel walls.

## 1. Introduction

The flow in a two-dimensional channel with a moving indentation in one wall has recently been studied experimentally (Stephanoff *et al.* 1983; Pedley & Stephanoff 1985) and numerically (Ralph & Pedley 1988), as a step towards understanding unsteady, separated, internal flows in general, and self-sustained oscillations in flexible-walled tube flows in particular. (The above papers will hereinafter be referred to as I, II and III, respectively.) The indentation was made to oscillate sinusoidally between a flush and an indented position. The experiments revealed the generation of a train of vorticity waves downstream of the indentation, with closed eddies between the crests/troughs of the wave and the wall. Under some circumstances certain of these eddies split, each into a pair of corotating parts ('eddy doubling').

† Present address: Smith Associates Ltd., Surrey Research Park, Guildford, Surrey GU2 5YP, UK.

All these features were reproduced by the Navier–Stokes solutions of III, at three different pairs of values of the Reynolds number $Re(=aU_0/\nu$, where $a$ is the undisturbed channel width, $U_0$ is the average velocity of the flow upstream and $\nu$ is the kinematic viscosity of the fluid) and Strouhal number $St(=a/U_0T$ where $T$ is the oscillation period); in each case the amplitude parameter $\epsilon$ was held fixed at 0.38.

In I and II an inviscid, small-amplitude theory was proposed which correctly reproduced the generation and propagation of vorticity waves but could not explain the formation of the closed eddies or the eddy doubling. Quantitative comparison of the theory with experiment was made by plotting the locations of the wave crests and troughs (hereinafter referred to simply as 'crests') in the form of graphs of their longitudinal coordinates $ax_c$ (relative to the end of the indentation) as functions of time $t$. The theory suggested that the results should be of the form

$$x_c St^{\frac{1}{3}} = f(t; \epsilon_1),$$

where $\epsilon_1 \propto \epsilon St^{-\frac{2}{3}}$ is a measure of amplitude and $f$ is a dimensionless function which depends only very weakly on $\epsilon_1$. The theory being inviscid, no dependence on $Re$ was predicted.

The experimental results indeed indicated no systematic dependence of $x_c$ on $Re$ (for $480 \leqslant Re \leqslant 950$) for any value of $St$ in the range 0.007 to 0.057 (figures 9 and 11 of II). They also confirmed that $x_c St^{\frac{1}{3}}$ was independent of $St$ in that range, but only during the first half of the cycle ($t \leqslant 0.5$); later in the cycle, the values of $x_c St^{\frac{1}{3}}$ increased with $t$ less rapidly for larger values of $St$ (e.g. figure 12 of II). Good quantitative agreement between theory and experiment (and Navier–Stokes solutions) was achieved throughout the cycle for the more upstream waves at the largest value of $St$ examined (0.057; see figure 16 of II and figure 13 of III), but the more downstream waves were not as far downstream as predicted. Thus the wavelength was overestimated in the theory although the phase velocity was well predicted, at larger $St$. At smaller $St$ the phase velocity was underestimated (figure 18 of II).

These results have led us to conclude that the wave generation and propagation process is essentially inviscid, and is not greatly affected by the viscous processes taking place in the eddies, as discussed in III. However, significant questions still remain. In particular, are the quantitative disagreements between the simple theory and the actual waves a consequence of the neglect of viscosity, as suggested by the fact that agreement is worse at the lower values of $St$, when the dynamics might be expected to be more quasi-steady and viscosity can therefore not be neglected? Alternatively, are they primarily caused by the small-amplitude assumption in the theory, with viscosity unimportant at all $St$, as suggested by the Reynolds-number independence of the experimental results? The fact that the theory was based on a series expansion in powers of $\epsilon$ that was truncated at $O(\epsilon^2)$ has two apparently distinct consequences. One is the obvious one that the fully nonlinear waves are likely to be severely distorted from the predictions of a weakly nonlinear theory, leading to considerable errors in the predictions of phase velocity and wavelength. The other stems from the fact that the in-and-out movement of the indentation must be accompanied by a bulk acceleration and deceleration of the flow downstream or upstream (or both). In the experiments and in the Navier–Stokes solutions of III the upstream flow rate was held constant. However, the theory takes no account of this effect, because it does not come in until the next order in $\epsilon$ (but see the footnote in §7.1), so there could be better agreement between the theory and a Navier–Stokes solution in which the downstream flow rate is held constant.

The aim of the present work is to try to answer the above questions, and further elucidate the physical mechanisms underlying the flows in question, by obtaining numerical solutions of the inviscid Euler equations for direct comparison with numerical solutions of the viscous Navier–Stokes equations with the same parameter values and the same up- and downstream conditions. Since agreement between experiment and Navier–Stokes solutions (for a range of $Re$ and $St$) have been established in III, we concentrate here on one particular case, called 'run 4' in II and 'case I' in III, with $St = 0.037$ and (for the Navier–Stokes solution) $Re = 507$.

The geometry and formulation of the problem are similar to those given in III, with the differences being described in §2, below; in §3, the finite-difference methods used are described. The results are presented and discussed in §§4, 5 and 6; in §4 we give the inviscid flow patterns with $\epsilon = 0.38$ and the upstream flow rate fixed, for comparison with the viscous results of III; in §5 we retain the same fixed amplitude and investigate the changes in the results when the downstream flow rate is held fixed; in §6 we examine the effects of varying $\epsilon$. Further discussion and conclusions are presented in §7.

## 2. Formulation

The formulation follows III very closely, and we use the same notation here. The computational domain is shown in figure 1; the walls of the channel are given by $y = 1$ and $y = F(x,t) \equiv g(x)\,h(t)$, where $h(t) = 0$ for $t < 0$, $h(t) = \frac{1}{2}(1-\cos 2\pi t)$ for $t \geqslant 0$, and $g(x) = 0$ for $x \leqslant x_2$ and $x \geqslant x_5$, $g(x) > 0$ for $x_2 < x < x_5$ ($g(x)$ is specified precisely in equation (17) of III). The domain is made steady and rectangular by means of the transformation $z = (y-F)/(1-F)$, and the Navier–Stokes equations, in terms of stream function $\psi$ and vorticity $\zeta$, become

$$\frac{\partial \zeta}{\partial t} = -\frac{1}{St} p_1 \left( \frac{\partial \psi}{\partial z}\frac{\partial \zeta}{\partial x} - \frac{\partial \psi}{\partial x}\frac{\partial \zeta}{\partial z} \right) + p_4 \frac{\partial \zeta}{\partial z} + \frac{1}{\alpha^2}\nabla^2 \zeta \tag{1}$$

and

$$-\zeta = \nabla^2 \psi, \tag{2}$$

where $p_1(x,t)$ and $p_4(x,z,t)$ depend on $F(x,t)$ and its derivatives; two other functions $p_2$ and $p_3$ arise in the transformation of the $\nabla^2$ operator (see III for details). The Euler equations are identical except for omission of the viscous term, proportional to $1/\alpha^2$, in (1). The initial condition is that there is Poiseuille flow everywhere, with

$$\psi = z^2(3-2z), \quad \zeta = 6(2z-1). \tag{3}$$

III deals only with cases in which the flow rate upstream of the indentation is fixed, and, where such flows are considered here, the value of the stream function on the indented wall $z = 0$ is given by

$$\psi = -St \int_{x_1}^{x} g(x')\,\mathrm{d}x' \frac{\mathrm{d}h}{\mathrm{d}t}, \tag{4}$$

while $\psi = 1$ on $y = z = 1$. For flows in which the downstream flow rate is to be held constant, this equation is replaced by

$$\psi|_{z=0} = -St \int_{x_5}^{x} g(x')\,\mathrm{d}x' \frac{\mathrm{d}h}{\mathrm{d}t} \tag{5}$$

in which the integral takes negative values for points on and upstream of the indentation ($x < x_5$) and is zero downstream ($x > x_5$). Thus, the stream function on

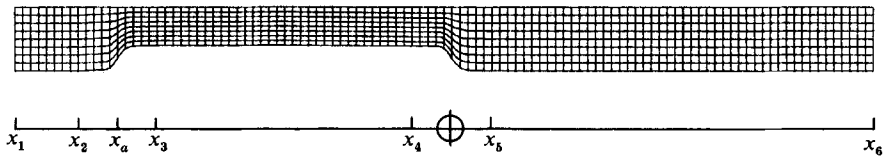


FIGURE 1. Representation of the computational domain. Lines of constant $x$ and constant $z$ are shown at the time of maximum indentation, and the $y$-scale is expanded by a factor of 2 compared with the $x$-scale. (From III).

the indented wall is greater than zero for $x < x_5$ when the piston is advancing into the channel, and, since $\psi$ is held constant at a value of unity on the other wall, this corresponds to the required reduced upstream flow rate. The boundary conditions far upstream and downstream require parallel flow and Poiseuille flow respectively when the downstream flow rate is fixed; the two are transposed, as in III, when the upstream flow rate is fixed.

## 3. Numerical methods

The finite-difference methods used to solve the Navier–Stokes equations for viscous flow were identical with those employed in III, except when simulating flows in which the downstream flow rate was held fixed. The small changes necessitated in such cases are described in §3.1, below.

The method of solution of the Euler equations governing the inviscid problem was developed from that used to solve the Navier–Stokes equations, and thus a stream function–vorticity formulation was employed with central, second-order spatial differences in the vorticity transport and stream function equations. The Poisson equation for the stream function was solved as in III, whilst the schemes employed for the vorticity transport equation are given in §3.2, below. The numerical boundary conditions are described in §3.3.

### 3.1. *Viscous flows with downstream flow rate fixed*

The numerical boundary conditions at the inlet boundary, $x = x_1$, were obtained by assuming the flow there to be parallel with the unindented channel walls. This gives rise to a one-dimensional diffusion equation for the vorticity at inlet, which was updated using central space differencing and leapfrog time differencing with the Dufort–Frankel substitution, as for internal points. Wall values of vorticity at inlet were obtained by a first-order evaluation of $\partial^2\psi/\partial z^2$. Nodal values of the stream function at $x = x_1$ satisfied a tridiagonal system, which was solved by the usual algorithm (see Roache 1976, for example), whilst values of $\psi$ on the lower wall were obtained by evaluating equation (1) at each wall node. Otherwise, solutions for flows in which the downstream flow rate was held fixed were obtained in the same way as for those in which the upstream flow rate remained constant (see III).

### 3.2. *The vorticity transport equation in inviscid flow*

Central, second-order space differencing and explicit, leapfrog time differencing were used in the vorticity transport equation, as for the viscous problem in III (the Dufort–Frankel substitution being unnecessary in the absence of diffusive terms). With a mesh spacing, $h$, of $\frac{1}{32}$, and a typical time-step size, $k$, of 1/4000, this method gave apparently stable solutions and smooth instantaneous streamline plots. However, inspection of the corresponding vorticity contour plots showed the

presence of spatial oscillations in vorticity, with a wavelength on the grid scale and an amplitude which was a significant fraction of the vorticity range. The use of an alternative time-differencing method (second-order Adams–Bashforth) and of time-like filters had little effect on the oscillations, and it was concluded that they were 'wiggles', as described in Roache (1976), resulting from the use of central differences in space in the presence of large vorticity gradients.

In order to eliminate the oscillations, a spatial filter was employed, but, since a principal objective of the study was to investigate differences between viscous and inviscid flows, it was important to use a method that would not be equivalent to simply introducing viscosity. The technique adopted was that used by Myers, Taylor & Murdock (1981) in pseudo-spectral inviscid flow calculations. Under this scheme, changes in the vorticity, $\zeta$, due to convection in the $x$-direction were computed first, and then filtering in this direction was carried out only where oscillations on the grid scale were found. Vorticity changes due to $y$-direction convection were then calculated and the required filtering again carried out. Details of the filtering techniques are described in the appendix: we may note that computations with filtering required about twice as much computer time as unfiltered runs. The results show a large reduction in the amplitude of the wiggles, although the vorticity variation is still not completely smooth (see figures 2*b* and 4, below).

As a check on the numerical accuracy of the scheme, and in order to verify that the spatial oscillations were indeed an artifact, filtered and unfiltered calculations were carried out with three different mesh sizes, $h = \frac{1}{24}$, $h = \frac{1}{32}$ and $h = \frac{1}{48}$, for a typical flow. In each of the unfiltered runs, the wiggles had a wavelength of $2h$, showing them to be unphysical, as expected. Their effects on the overall flow structure were small, however, and comparison of the variation with $x$ of the centreline stream function, $\psi_{\mathrm{CL}}$, showed very little effect of changes in mesh size or of the presence or absence of filtering. Filtered results for a typical time in the flow cycle are shown in figure 2(*a*).

Figure 2(*b*) shows the variation with $x$ (for $x > 0$) of the vorticity, $\zeta_1$, at $z = 0.875$ in filtered calculations for the three mesh sizes given above. All the curves show some residual wiggles, although the amplitude of these is small compared with the vorticity range. The abrupt peaks near $x = 2.5$ and $x = 5.5$ appear to be genuine features, since they occur for each mesh size, and become more acute as the mesh is refined. We regard the vorticity curves for the two finest meshes as being close enough to indicate that reasonably accurate solutions may be obtained by utilizing the mesh size $h = \frac{1}{32}$: all the results given below have been obtained using such a grid, in filtered computations. Finally, we note that in inviscid flow the vorticity should be bounded by the range of initial values and those imposed at the inflow boundaries, that is, the range $-6$ to $+6$ in the present problem. Whilst discretization errors may cause these bounds to be exceeded (maximum and minimum vorticity values in a typical case are given in the legend for figure 4, below, showing values of $|\zeta|$ up to 6.8), this only occurs in very small, isolated regions of the solution domain, mainly within eddy A; in the 'worst case' of $t = 0.75$, $|\zeta| \geqslant 6.2$ at fewer than 0.3% of the nodes.

### 3.3. *Boundary conditions in inviscid flow*

Boundary values of the stream function, $\psi$, in inviscid flow were determined just as for viscous flow, and no further description is given here. On the other hand, the boundary vorticity requires different treatment. At $x = x_1$, which in all flows is a mean inlet boundary, the vorticity profile is taken to be linear, corresponding to Poiseuille flow at the mean flow rate. This gives a parabolic velocity profile, with a time-varying slip velocity at the walls in the cases of non-constant upstream flow

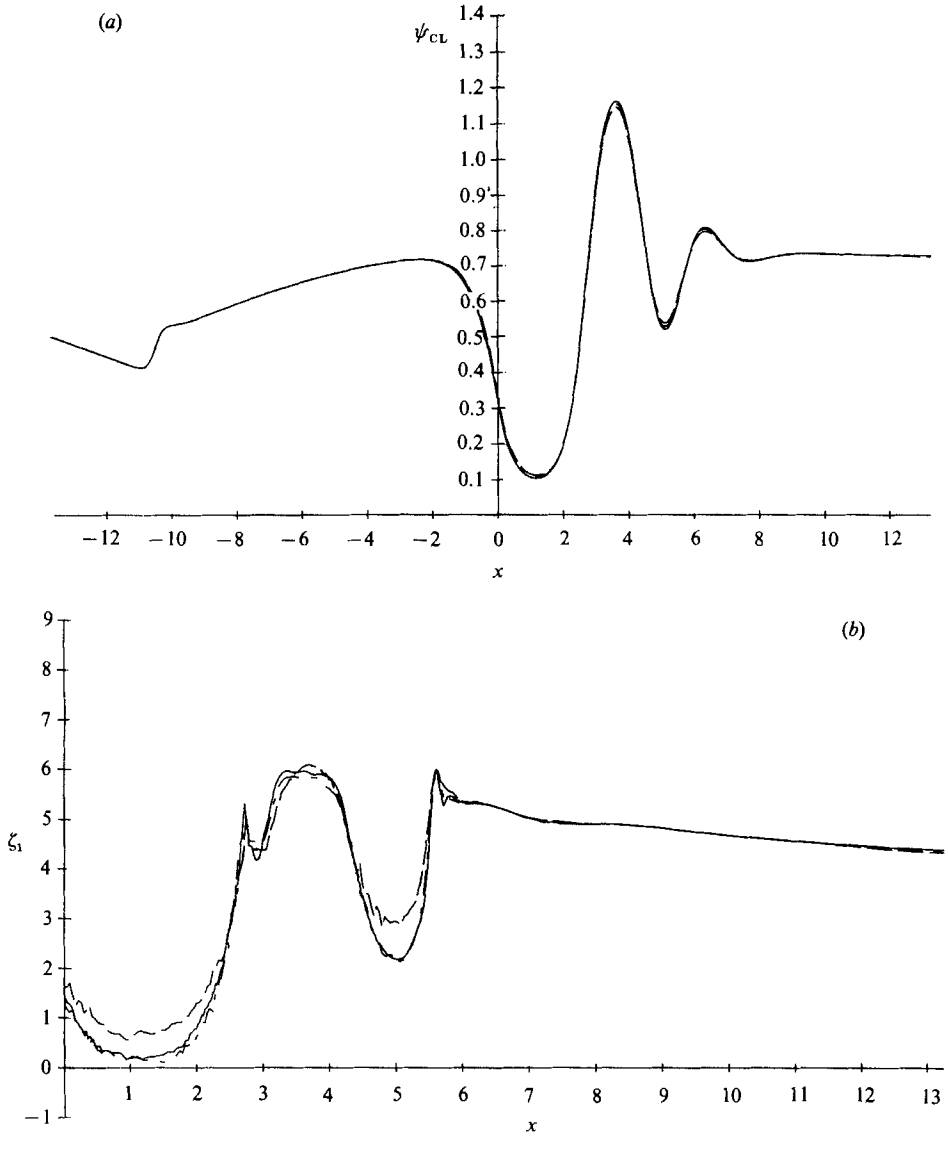


FIGURE 2(*a*, *b*). For caption see facing page.

rate. The downstream boundary condition of III was found to lead to instability when applied at $x = x_6$ in inviscid flow calculations, and was replaced by a method based on that of Shapiro & O'Brien (1970). Under this scheme, the positions at the previous time step of fluid particles currently situated at outlet nodes are first determined by interpolation of the local velocity field. The vorticity carried by each particle is then calculated by interpolation based on its position in the 'old' vorticity field: since fluid elements retain their vorticity in inviscid flow, the vorticity assigned to each outlet node is simply that of the corresponding fluid particle at the previous time step. Where the axial velocity is negative at $x = x_6$, Poiseuille flow values of vorticity are assigned to the relevant nodes. To assess the effects of imposing the boundary conditions at a finite distance from the indentation, a computation was carried out in which the upstream and downstream boundaries were moved upstream

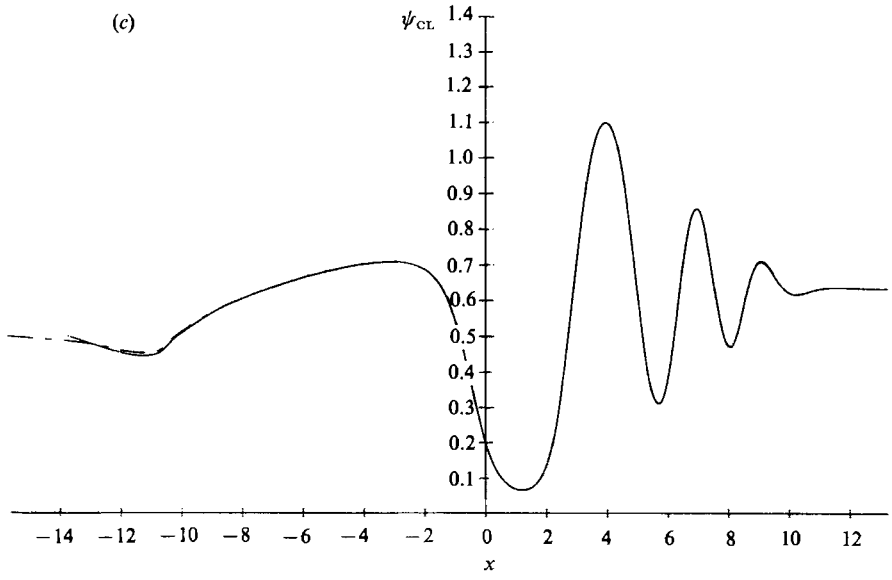


FIGURE 2. (*a*) Variation of the centreline stream function with axial position at $t = 0.75$ in a typical inviscid flow ($St = 0.037$, $\epsilon = 0.38$, upstream flow rate fixed): $h = 1/48$ (solid curve); $h = 1/32$ (long-and-short-dashed curve); $h = 1/24$ (long-dashed curve). (*b*) Variation of vorticity at $z = 0.875$ and $t = 0.75$ in the same flow, with the same mesh sizes as in (*a*). (*c*) Variation of centreline stream function in the same flow at $t = 0.90$ with $h = 1/32$; $x_1 = -13.75$, $x_6 = 13.25$ (solid curve); $x_1 = -15.75$, $x_6 = 11.25$ (dashed curve).

by two channel widths from the locations used throughout the rest of this work ($x_1 = -13.75$, $x_2 = 13.25$). The results are illustrated in figure 2(*c*) for a time $t = 0.90$. It can be seen that in the region of primary interest ($x > 0$) the effect of the shift in the upstream boundary is undetectable on this plot, whilst that of the downstream boundary shift is small and confined to the vicinity of $x_6$. In discussing the results below, we restrict attention to $x < x_6 - 2$, and we are confident that they are unaffected by the computational boundary positions.

Values of vorticity at the walls are determined using a one-sided finite-difference form of (2). However, since the no-slip condition is not applicable in inviscid flow, this equation cannot be simplified in the same way as in the viscous case; in particular, the Woods boundary condition (Roache 1976, p. 141) cannot be applied. A first-order scheme was therefore adopted.

## 4. Results: comparison of viscous and inviscid flows

Instantaneous streamlines for a typical inviscid flow, in which the upstream flow rate is held fixed, are given in figure 3. The contour values of the stream function have been selected according to (23)–(25) of III, and $\psi_{max}$, $\psi_{min}$ and $\psi_w$ are as defined there. The parameter values are such as to permit direct comparison with the viscous flow depicted in figure 4 of III. Many features of the inviscid flow are similar to those observed experimentally and predicted by the Navier–Stokes calculations. Thus, the core flow downstream of the indentation becomes progressively wavy, and the front of the wave eventually propagates much more rapidly than any individual crest or trough. Furthermore, regions with closed streamlines ('eddies') develop between the crests/troughs and the wall, and each of these grows in lateral extent until it occupies

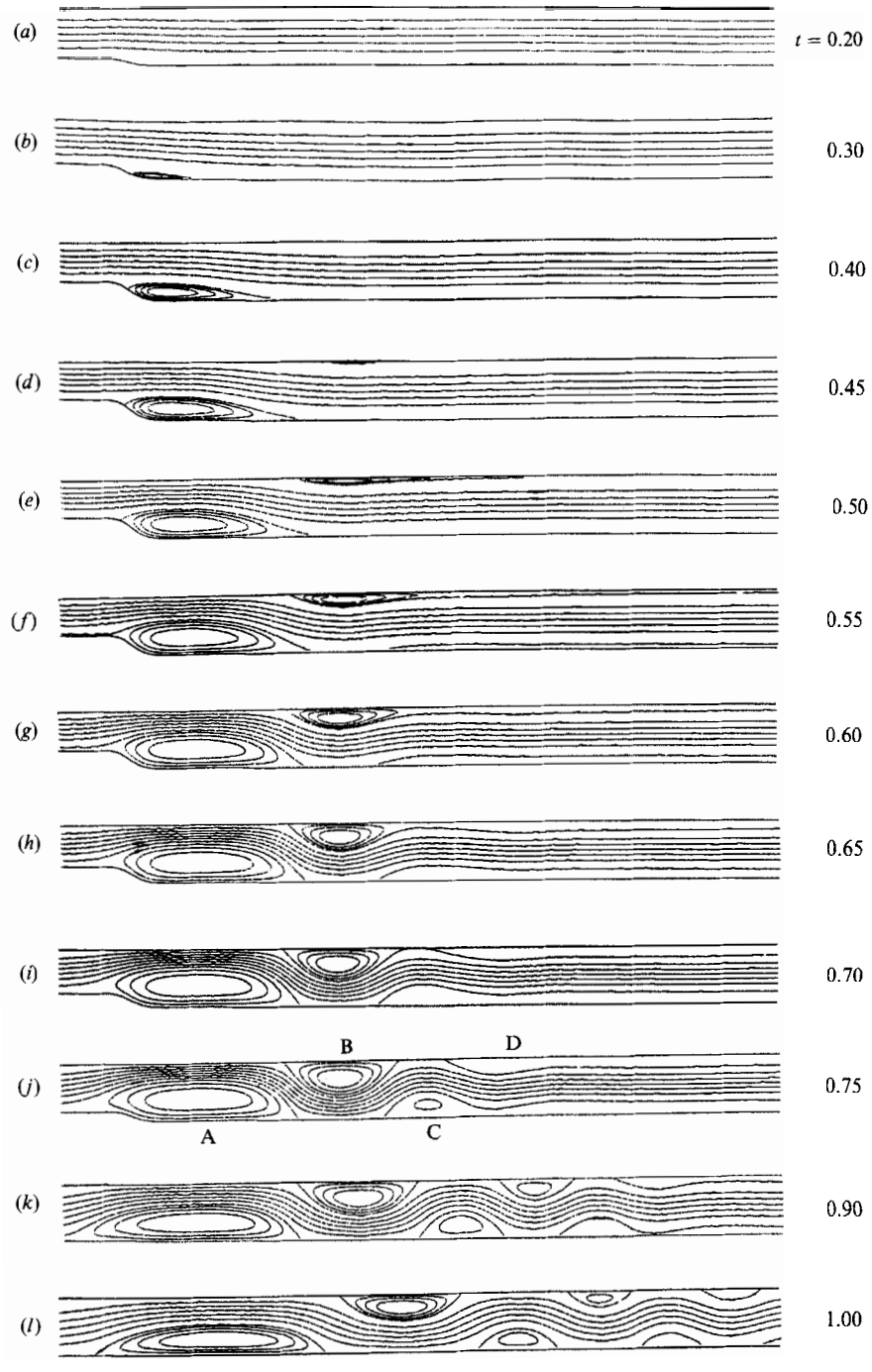


FIGURE 3. Instantaneous streamline plots for a typical inviscid flow ($St = 0.037$, $\epsilon = 0.38$, upstream flow rate fixed): (*a*) $\psi_{max} = 1.000$, $\psi_{min} = -0.441$, $\psi_w = -0.441$; (*b*) 1.000, −0.464, −0.464; (*c*) 1.000, −0.337, −0.273; (*d*) 1.001, −0.258, −0.143; (*e*) 1.011, −0.180, 0; (*f*) 1.038, −0.086, 0.143; (*g*) 1.084, −0.043, 0.273; (*h*) 1.148, 0.012, 0.375; (*i*) 1.206, 0.049, 0.441; (*j*) 1.244, 0.064, 0.464; (*k*) 1.215, −0.026, 0.273; (*l*) 1.139, −0.193, 0.

about half of the channel width. Thus the generation of eddies is not a necessarily viscous process.

There are, however, several respects in which the inviscid flow differs from the viscous case. The development of significant amplitude in the more downstream waves seems to be delayed in the inviscid case, and eddy B does not propagate significantly between about $t = 0.45$ and $t = 0.75$. The remaining differences are primarily concerned with the shapes and structures of the eddies, labelled for convenience as in figure 3(*j*). Thus, eddy A, in the inviscid case, grows to become significantly larger in lateral (though not longitudinal) extent than the corresponding eddy in viscous flow. All of the eddies show a much greater degree of fore-aft symmetry in inviscid flow, and there is certainly no eddy doubling or even kinking of the dividing streamlines. On the other hand, there is not a great difference in the eddy strengths during the middle part of the flow cycle in the two cases, and at $t = 0.60$, for example, the value of $(\psi_{\max} - 1)$, representing the strength of eddy B, is 0.109 in the viscous case and 0.084 in the inviscid case: in the inviscid case, however, the eddy strength continues to increase until rather later in the flow cycle, attaining its maximum value of 0.254 at $t = 0.80$, compared with $t = 0.60$ in the viscous flow. We also note that there is no decay in the amplitude of the wave or the strengths of the eddies near the end of the inviscid flow cycle, nor do the eddies appear to be swept away downstream; there is no mechanism for damping the wave in inviscid flow. This means that after more than one cycle the inviscid flow will be different from that computed here, just one cycle after the initial state of unperturbed Poiseuille flow. However, it is differences between the viscous and inviscid development of the flow during the first cycle that are relevant here.

In unsteady flow, instantaneous streamlines and vorticity contours are not necessarily coincident, as they are in steady inviscid flow. The vorticity contour plots corresponding to figure 3 are given in figure 4, and can be compared with the viscous flow results shown in figure 8 of III. The method of determining contour values of the vorticity was the same as that used in III.

There is approximate coincidence of streamlines and vorticity contours in the flow near the centre of the channel, which suggests that the flow there is essentially quasi-steady. A measure of the importance of unsteadiness in a flow is the local Strouhal number, i.e. lengthscale divided by frequency times typical local velocity; in the centre of the channel this is comparable with the overall Strouhal number, *St*, which is small, consistent with quasi-steady flow. Nearer the walls, however, the local velocity is small so the local Strouhal number is not, and it is therefore not surprising to observe significant differences between streamlines and vorticity contours.

It should be noted that, in inviscid flow, vorticity contours are identified with material lines, and thus no breaking of these contours is possible. However, owing to the finite resolution of the grid, contour breaking does occur in our computations when material lines are sufficiently 'wound up' by nonlinear processes. This is not believed to affect the overall flow structure since the size of the grid, which determines when contour breaking occurs, does not itself affect the structure significantly.

It is of interest to consider the vorticity dynamics of a single, typical eddy, eddy B, say. We observe initially a local thickening of the region of high vorticity near the wall (figure 4*a–c*), and this process leads to the formation of closed streamlines (figure 3*d*). As the thickening continues, the vorticity in the area bounded by closed streamlines remains almost uniform until about $t = 0.60$ (figure 4*g*). Subsequently, strips of fluid from the core are wound convectively about the eddy centre,

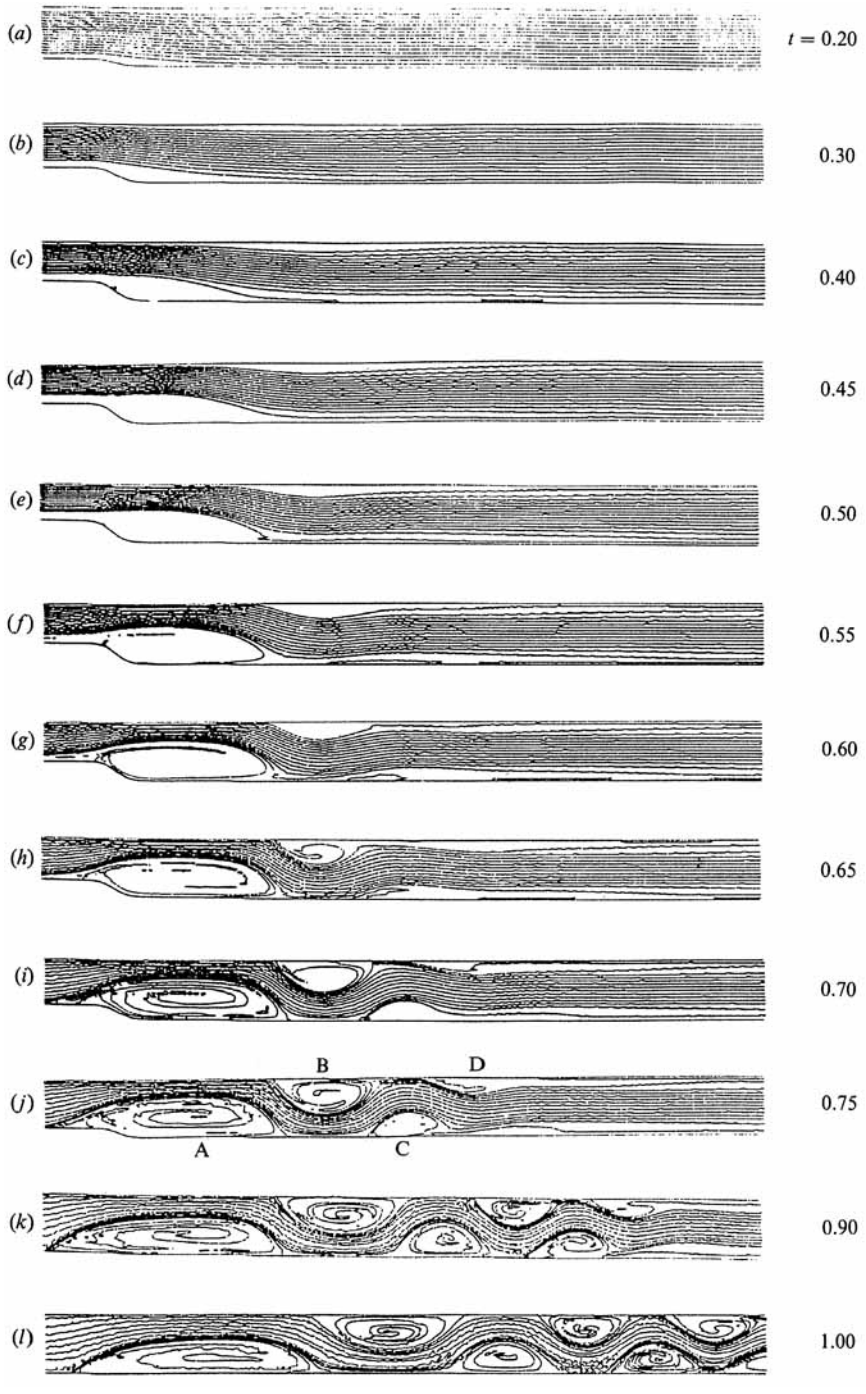


FIGURE 4. Instantaneous vorticity contour plots for a typical inviscid flow ($St = 0.037$, $\epsilon = 0.38$, upstream flow rate fixed): (*a*) $\zeta_{max} = 5.67$, $\zeta_{min} = -6.00$; (*b*) 5.71, −6.11; (*c*) 5.74, −6.44; (*d*) 5.77, −6.13; (*e*) 5.86, −6.26; (*f*) 6.06, −6.37; (*g*) 6.11, −6.40; (*h*) 6.41, −6.40; (*i*) 6.14, −6.80; (*j*) 6.25, −6.80; (*k*) 6.50, −6.76; (*l*) 6.74, −6.65.

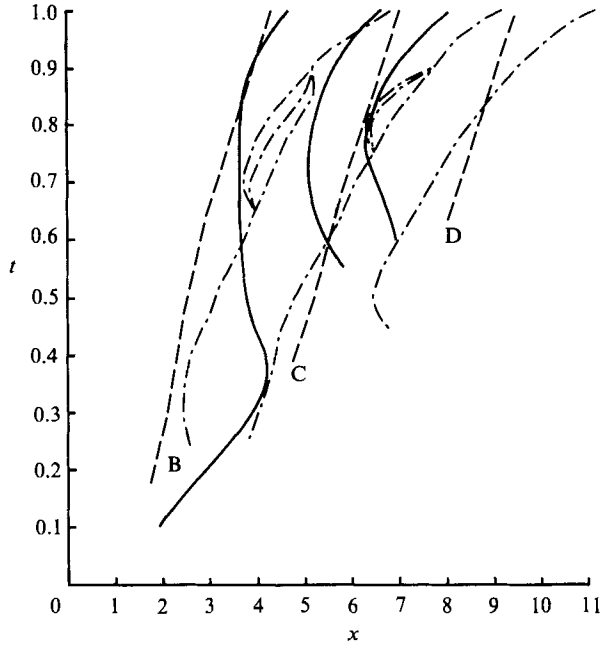


FIGURE 5. Positions of crests/troughs corresponding to eddies B, C and D as functions of time in flows with $\epsilon = 0.38$ and $St = 0.037$, and with upstream flow rate fixed. Solid curves and dash-dotted curves show numerical results for inviscid and viscous ($Re = 507$) flow, respectively. The dashed curves show the predictions of the simple theory. The trifurcations in the viscous curves indicate multiple turning points in the centreline stream function, corresponding to incipient and actual eddy doubling (see III).

representing a strongly nonlinear process. Artificial (numerical) contour breaking then leads to closed vorticity contours being created (e.g. eddies A and C in figure 4*l*).

Finally, we can make a quantitative comparison between the viscous and inviscid solutions, and the small-amplitude inviscid theory of I and II, by plotting the positions of the wave crests as functions of time. In the theory a crest is defined as a turning point of the displacement function $A(x, t)$, while in the numerical solution it is identified with a turning point of the axial variation in the centreline stream function. In figure 5 the positions of the crests corresponding to eddies B, C and D are plotted. We can see that the full Euler solution does not agree well with the small-amplitude inviscid theory, except insofar as the mean phase velocity of the waves is close to its theoretical value. The wavelength however is shorter than in the viscous flow (especially late in the cycle) whereas the theory gave larger values. Also a quasi-sinusoidal oscillation in crest position is superimposed on the average phase velocity. These results indicate that finite-amplitude effects are important, and the oscillation in particular suggests that the acceleration and deceleration of the downstream flow is a major source of disagreement between the Euler solution and the theory (see the footnote in §7.1).

However, agreement with the viscous solution is also poor, indicating a significant effect of viscosity despite the Reynolds-number independence of the experimental (viscous) crest positions. This is further discussed below.

## 5. Results: effect of up- or downstream flow acceleration

As in the last section, we first discuss the computed flow patterns (in the form of streamline plots) to investigate any qualitative differences that might be attributable to bulk acceleration/deceleration upstream as opposed to downstream. We than go on to examine quantitative differences in crest positions.

In the case of an inviscid fluid the flow structure with downstream flow rate fixed is qualitatively very similar to that with upstream flow rate fixed. With $St = 0.037$ and $\epsilon = 0.38$, as for figure 2, the amplitude and wavelength of the wave are the same as shown there. The only difference lies in the rate of axial growth of eddy A, which is less rapid, during the first half of the flow cycle, in the case with the downstream flow rate fixed. This leads to a slower rate of propagation of the crests/troughs further downstream, and is accompanied by a reduced speed of propagation of the wave front (see figure 7, below). The lack of any significant effect is not surprising because acceleration of the bulk flow, in a parallel-sided region of the channel located further than $O(a)$ from the indentation, merely involves the superposition of a time-dependent but spatially uniform velocity on to the previously existing flow. The vorticity distribution will remain unchanged, relative to a frame of reference moving with this velocity.

In viscous flow, the differences between flows with fixed up- and downstream flow rates are more marked. Figure 6 shows instantaneous streamline plots in a typical flow with constant flow rate downstream of the indentation, and the parameters precisely match those of the flow shown in figure 4 of III, which differs only in that the upstream flow rate is fixed in that case. First, and most importantly, we note that a vorticity wave and a number of eddies are clearly seen in figure 6, proving, as was thought to be the case, that the wave does not rely on the destabilizing effect of deceleration for its genesis. On the other hand, the wave amplitude increases much more slowly in figure 6 than in figure 4 of III, and never attains the magnitude shown there; furthermore the wave front propagates along the channel more slowly. The eddies are much less vigorous in the fixed-downstream-flow case: for example, at $t = 0.60$, $(\psi_{\max} - 1)$, representing the strength of eddy B, takes the values 0.015 and 0.109 in the fixed down- and upstream flow rate cases respectively. Finally, we note that the eddies shown in figure 6 do not exhibit doubling.

Thus, acceleration/deceleration of the viscous flow downstream of the indentation is seen to result in an amplification of the vorticity wave and a strengthening of the associated eddies. At least two mechanisms may be causally involved in this effect. First, there is enhanced generation of vorticity at the walls for $t < 0.25$, compared with the fixed downstream flow rate case, because the acceleration of the flow generates an increased wall shear rate. This vorticity presumably contributes to the strengths of the eddies. Secondly, the flow downstream of the indentation is decelerating for $t$ between 0.25 and 0.75, and deceleration of channel or boundary-layer flows is well known to make them more unstable, at least in linear theory, with much more rapid growth of Rayleigh or Tollmien–Schlichting waves, because of the presence of a point of inflection in the velocity profile (Obremski, Morkovin & Landahl 1969; Hall & Parker 1976; Gad-el-Hak *et al.* 1984). As discussed in II and III, our vorticity wave can be thought of as a form of Tollmien–Schlichting wave. Moreover, Sobey (1980, 1983) studying flow in wavy-walled channels, has shown that finite-amplitude eddies grow more rapidly during deceleration, the rate of growth increasing with $St$.

The results for the crest positions corresponding to eddies B, C and D are presented

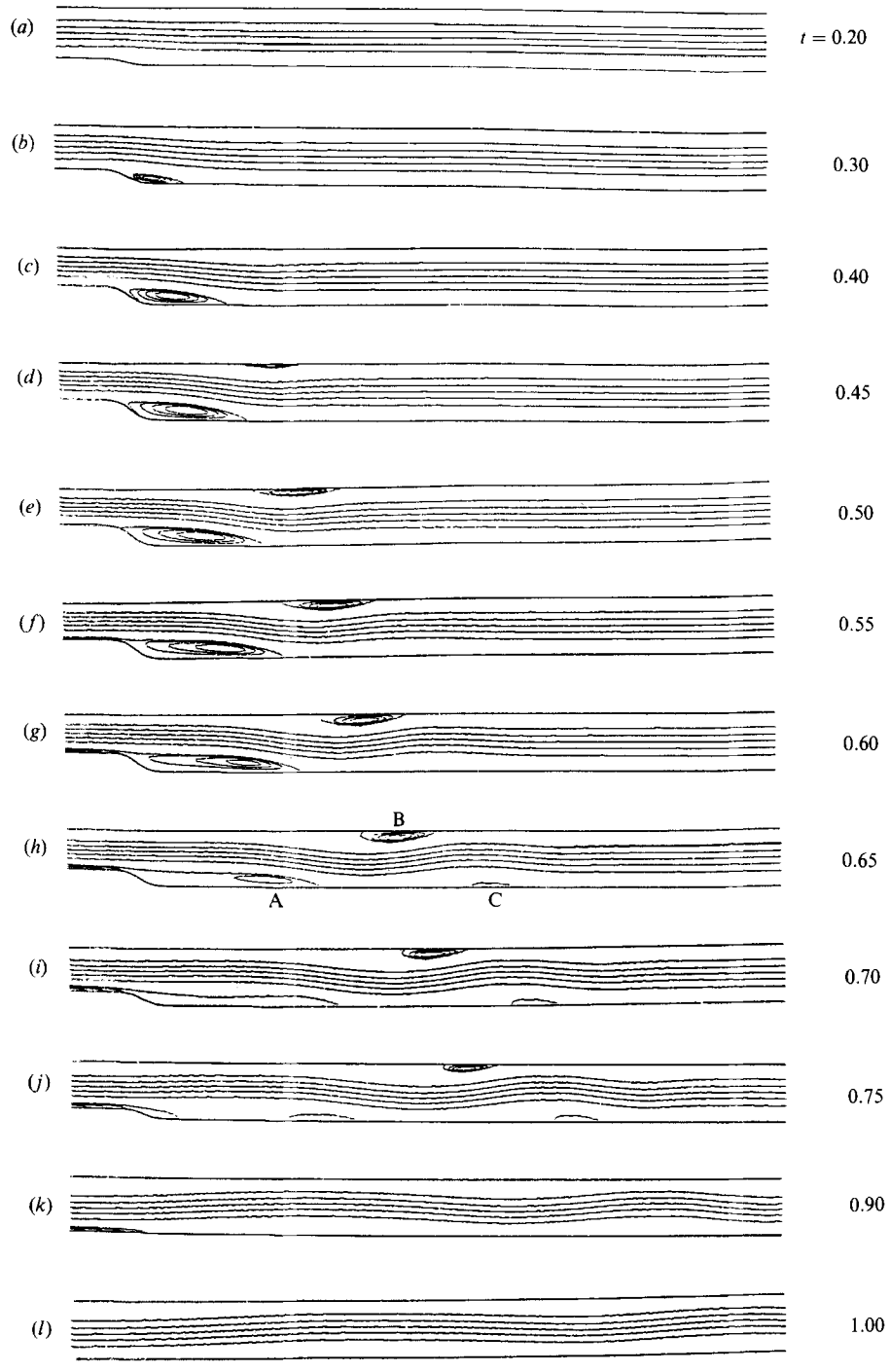


FIGURE 6. Instantaneous streamline plots for a viscous flow in which the downstream flow rate is fixed ($Re = 507$, $St = 0.037$, $\epsilon = 0.38$): (*a*) $\psi_{max} = 1.000$, $\psi_{min} = 0$; (*b*) 1.000, −0.005; (*c*) 1.000, −0.024; (*d*) 1.001, −0.032; (*e*) 1.004, −0.037; (*f*) 1.010, −0.035; (*g*) 1.015, −0.032; (*h*) 1.015, −0.045; (*i*) 1.011, −0.053; (*j*) 1.005, −0.055; (*k*) 1.000, −0.032; (*l*) 1.000, 0.

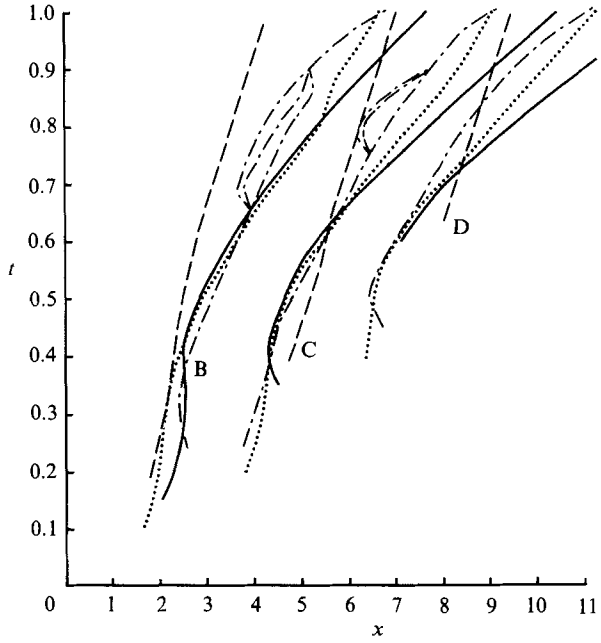


FIGURE 7. Positions of crests/troughs corresponding to eddies B, C and D as functions of time. Parameter values: $\epsilon = 0.38$, $St = 0.037$, $Re$(for viscous cases only) = 507. Dash-dot curves: Navier–Stokes solution, upstream flow rate fixed; solid curves: Navier–Stokes solution, downstream flow rate fixed; dotted curves: Euler solution, downstream flow rate fixed; dashed curves: small-amplitude inviscid theory.

in figure 7. As in figure 5, the dashed curves are the results of the small-amplitude inviscid theory, while the dash-dotted curves come from the Navier–Stokes solutions with upstream flow rate fixed, as in the experiments (the trifurcations in these curves represent eddy doubling, as discussed in III). Superimposed on these are the viscous (solid) and inviscid (dotted) curves for fixed downstream flow rate. The dimensionless parameters are unchanged. Considering first the viscous curves, we note that there is very little difference between the two cases, with upstream or downstream flow rate fixed, until about $t = 0.65$. Thereafter it is noticeable that the average phase speeds of the crests are greater when the downstream flow rate is fixed rather than pulsating, and that this leads to worse agreement with the simple theory.

Next we compare the viscous and inviscid results with downstream flow rate fixed, and this is particularly revealing because there is essentially no difference between the curves until late in the cycle, especially for eddy B. Keeping the downstream flow rate fixed means that the vorticity distribution present before the waves arrive at a particular location is the same in the two cases so this result reinforces the conclusion that wave generation and propagation does not depend on the presence of viscosity. It is also interesting that, when a discrepancy does develop, the waves propagate faster in a viscous fluid. A possible mechanism for this is discussed in §7. A consequence of this effect is that the inviscid results are in slightly better agreement than the viscous ones with the small-amplitude theory. Early in the flow cycle this agreement is very good (e.g. $t < 0.4$ for eddy B, $t < 0.3$ for eddy C), and certainly much better than for the inviscid case with upstream flow rate fixed (figure 5). Later in the flow cycle, however, none of the results agree well with the theory.

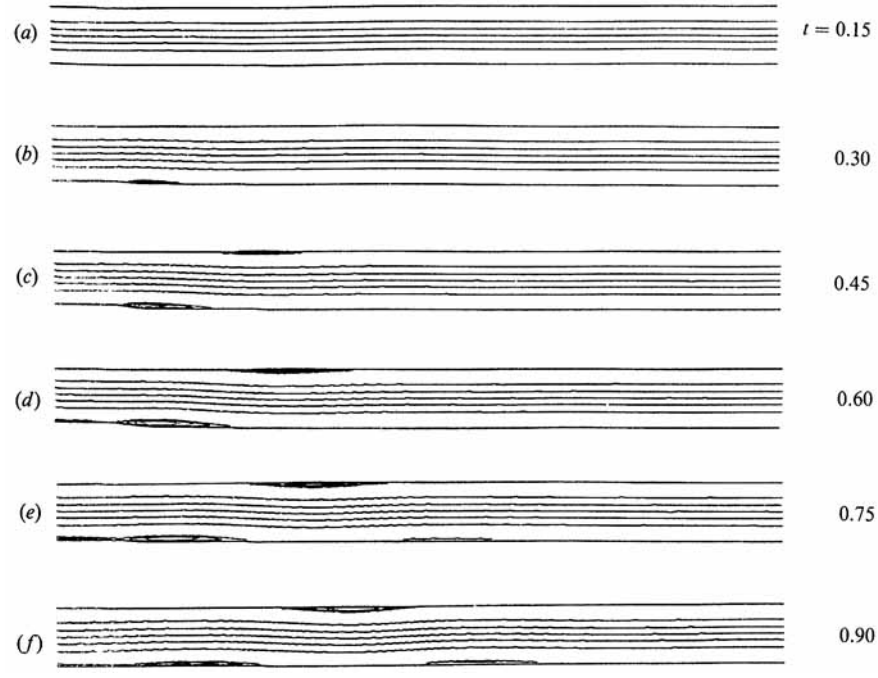


FIGURE 8. Instantaneous streamline plots for a small-amplitude inviscid flow with downstream flow rate fixed ($St = 0.037$, $\epsilon = 0.1$): (*a*) $\psi_{\max} = 1.000$, $\psi_{\min} = 0$; (*b*) 1.000, −0.003; (*c*) 1.001, −0.009; (*d*) 1.004, −0.014; (*e*) 1.006, −0.015; (*f*) 1.006, −0.009.

## 6. Results: effects of varying amplitude

As before, we consider the qualitative flow patterns first, and wave crest positions later. As $\epsilon$ is decreased, the amplitude of the wave decreases too, so that, for example, in viscous flow with upstream flow rate fixed and the same values of $Re$ and $St$ as in the flow of figure 6, all the eddies except for eddy A disappear when $\epsilon = 0.2$, although wave crests and troughs can still be detected. When $\epsilon = 0.1$, the wave itself is undetectable. In the corresponding flow with downstream flow rate constant, the core wave is weaker still for values of $\epsilon$ of 0.2 or less. Increasing $\epsilon$ leads to an increase in the amplitudes and strengths of the eddies, with $(\psi_{\max} - \psi)$ taking the value 0.216 at $t = 0.6$ in a flow with $\epsilon = 0.5$, $Re = 507$, $St = 0.037$ and upstream flow rate fixed, compared with 0.109 for $\epsilon = 0.38$.

In inviscid flow, waves and eddies are still found at the lowest value of $\epsilon$ considered, $\epsilon = 0.1$, with either up- or downstream flow rate fixed; figure 8 shows a flow under the latter condition. The transverse dimensions of the eddies are of the same order of size as $\epsilon$, whilst in axial extent they are, except for eddy A, somewhat larger than their counterparts in higher-amplitude flows (see figure 3, above). Eddy A is rather smaller in axial extent, and all of the eddies are weaker in the lower-$\epsilon$ case. Values of $\epsilon$ greater than 0.38 have not been considered in inviscid flow.

The effect of changing $\epsilon$ on the crest positions in viscous flow is shown in figure 9, where the results for $\epsilon = 0.2$ and upstream flow rate fixed are compared with the standard results for $\epsilon = 0.38$ ($Re$ and $St$ taking the same values as for figure 7) and with the small-amplitude inviscid theory. The main conclusion to be drawn is that, apart from the fact that individual crests are detected later when $\epsilon$ is smaller, the change in $\epsilon$ has very little effect. Reducing the amplitude in the Navier–Stokes

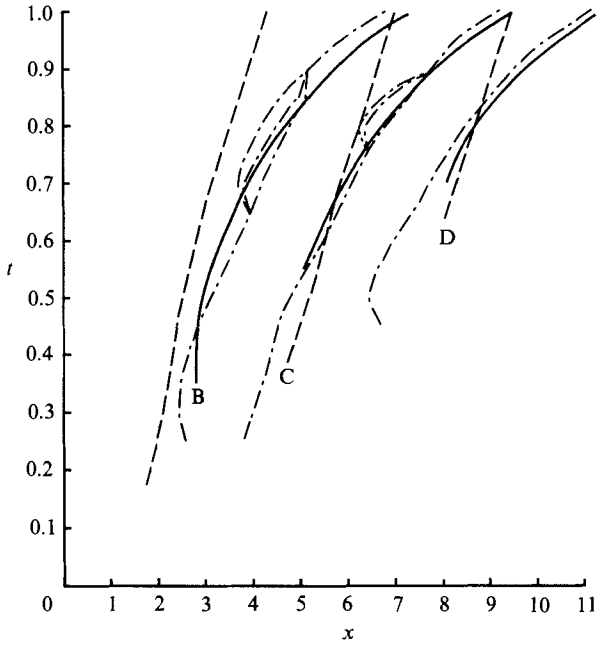


FIGURE 9. Positions of crests/troughs corresponding to waves B, C and D as functions of time in viscous flows with $Re = 507$, and upstream flow rates fixed. The solid and dash-dotted curves show numerical results for $\epsilon = 0.2$ and $\epsilon = 0.38$ respectively.

solution does not improve agreement with the theory. A similar result was observed experimentally (II, figure 11). A comparably small change was computed when $\epsilon$ was increased to 0.5, and a similarly weak dependence on $\epsilon$ was found when downstream flow rate was held fixed instead of upstream. Thus large-amplitude effects are unlikely to be the principal cause of the discrepancy between the theory and the full Navier–Stokes solutions. In particular, since eddies are found for $\epsilon = 0.38$ and not for $\epsilon = 0.2$, the wave crest positions do not appear to be significantly affected by the presence or otherwise of eddies.

In inviscid flow, on the other hand, changing the amplitude makes a big difference. This can be seen from figures 10 and 11, where the crest positions are shown for $\epsilon = 0.38$, $\epsilon = 0.2$ and $\epsilon = 0.1$ in the two cases of fixed upstream (figure 10) and downstream (figure 11) flow rate. (The same theoretical curves, calculated with $\epsilon = 0.38$, are included in all cases, because the dependence of crest positions on $\epsilon$, according to the theory, is extremely weak; see figure 18 of II.) In figure 10 the reduction in $\epsilon$ leads to improved agreement on crest mean phase velocities, though not on their positions, with the crests being shifted upstream in general. In figure 11, the effect of changing $\epsilon$ is clearly seen, with phase speeds being reduced dramatically as $\epsilon$ decreases, except in the early part of the flow cycle. Indeed, the predictions of the position of eddy B from the theory and inviscid numerical solutions for $\epsilon = 0.2$ are now in excellent agreement, and the phase velocities for all crests agree well at this amplitude. The wavelengths derived from the full Euler solution increase as $\epsilon$ decreases, but they remain somewhat shorter than those predicted by the theory, even at $\epsilon = 0.1$. In fact, the results at $\epsilon = 0.1$ show slightly worse agreement with the theory, at least for the position of crest B, than those at $\epsilon = 0.2$. Thus in seeking mechanisms to account for any discrepancies, we should expect that at least two

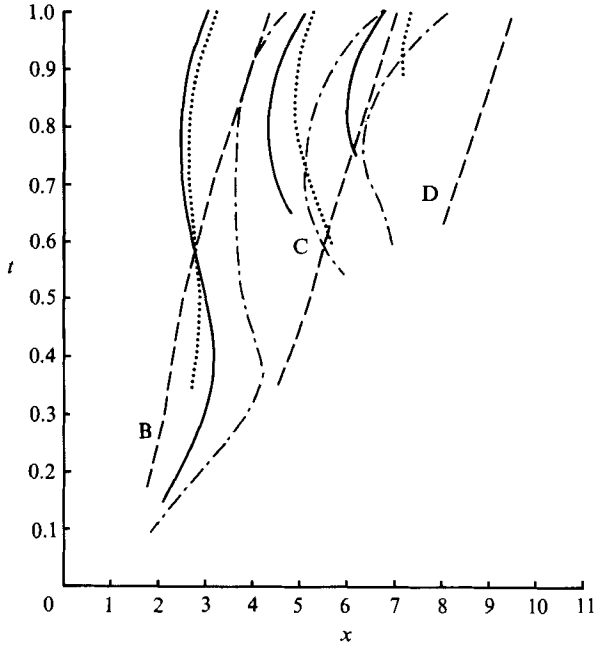


FIGURE 10. Positions of crests/troughs corresponding to eddies B, C and D as functions of time in inviscid flows with upstream flow rates fixed. The dash-dotted, solid and dotted curves show numerical results for $\epsilon = 0.38$, $\epsilon = 0.2$ and $\epsilon = 0.1$ respectively.

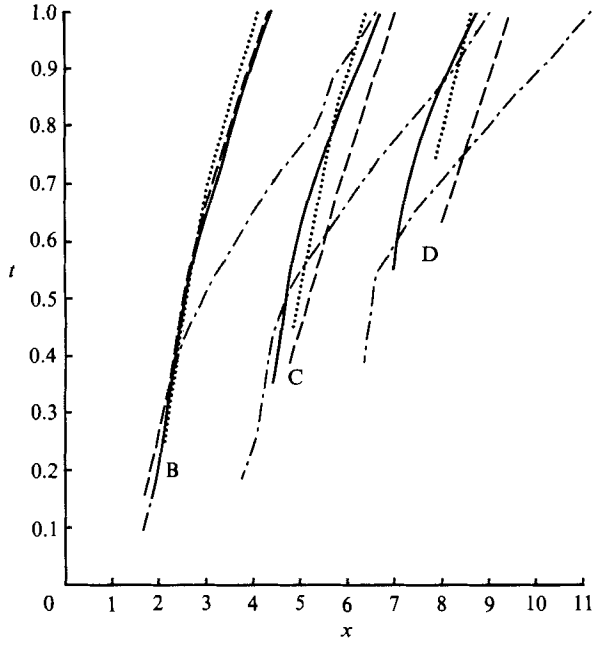


FIGURE 11. Positions of crests/troughs corresponding to eddies B, C and D as functions of time in inviscid flows with downstream flow rates fixed. The dash-dotted, solid and dotted curves show numerical results for $\epsilon = 0.38$, $\epsilon = 0.2$ and $\epsilon = 0.1$ respectively.

effects will be involved, acting in opposite senses and dominant at different amplitudes. Nonetheless, the degree of correspondence in figures 10 and 11 adds to our confidence in both the theory and the numerical procedure for the Euler equations.

Finally we note the marked contrast that exists between the viscous and the inviscid results. Figure 9 shows very little dependence of crest positions on $\epsilon$, whilst figure 11 exhibits a very strong amplitude effect. This difference is discussed below.

## 7. Discussion

The first conclusion of this paper is the confirmation that vorticity waves are generated downstream of a time-dependent indentation in an inviscid fluid as they are in a viscous fluid. Also, eddies are formed between the wave crests and the channel walls, although their structure is rather different from those found in the viscous case. In particular, eddy doubling does not occur in an inviscid flow, although this phenomenon is not purely viscous since, as argued in III, inviscid advection of vorticity plays a vital part, and thus a strong interaction of viscous and inviscid effects is involved in the process. In this section we further discuss possible reasons for the discrepancies between the inviscid, Euler equation solutions and (i) the small-amplitude theory, (ii) the viscous, Navier–Stokes solutions.

### 7.1. *Comparison between Euler solutions and theory*

The theory presented in I and II was also based on the Euler equations, coupled with a small-amplitude ($\epsilon$) and frequency ($St$) approximation which led to the leading-order perturbation to the oncoming parabolic velocity profile being a quasi-steady lateral displacement. This was represented by a function $A(x,t)$ which was shown at second order (in $\epsilon$) to satisfy the linearized Korteweg–de Vries equation, downstream of the indentation. The full Euler solutions indeed reveal quasi-steady flow in the core of the channel, where vorticity contours and streamlines are approximately coincident (figures 3 and 4), but there is a marked discrepancy near the wall, because the local Strouhal number is not small. Equivalently, the small-amplitude approximation of the theory is not uniformly valid near the wall because the unperturbed velocity tends to zero there and the perturbation does not. As shown in II, the leading, $O(\epsilon)$, terms of the inviscid small-$\epsilon$ expansion in the resulting critical layer at the wall are the same as assumed in the theory, but the error is $O(\epsilon^2 \log \epsilon)$ instead of $O(\epsilon^2)$. Thus a departure from the theoretical results is to be expected at finite $\epsilon$, but one might still expect it to diminish as $\epsilon$ becomes small, especially if the downstream flow rate is held fixed instead of the upstream. (As we have seen (figure 10), acceleration and deceleration of the downstream flow, although an $O(\epsilon^2)$ effect, causes a marked sinusoidal variation in wave crest position to be superimposed on that associated with the vorticity waves alone, even for $\epsilon = 0.1$†.)

† It has been pointed out by Dr S. J. Cowley that the sinusoidal acceleration and deceleration of the downstream flow can be incorporated into the small-amplitude theory at $O(\epsilon)$ if the dimensionless length of the indentation is formally taken to be $O(\epsilon^{-\frac{3}{2}})$ instead of $O(\epsilon^{-\frac{1}{2}})$. The equation governing the dimensionless core-flow displacement, equal to $\epsilon A(x,t)$, then becomes

$$A_{xxx} - l\pi \sin 2\pi t A_x - A_t = \tfrac{1}{2}F_t + \epsilon_1(FF_x + AF_x + FA_x), \tag{6}$$

where $\epsilon F(x,t) = \epsilon g(x)\, h(t)$ is the wall displacement and $l = \epsilon(10St)^{\frac{1}{3}} \int_{-\infty}^{\infty} g(x)\, dx$. This differs from equation (17) of II by the inclusion of the second term. In the region downstream of the indentation, where $F \equiv 0$, (6) is the same linearized Korteweg–de Vries equation as analysed in II,

Figure 11 indeed shows a dramatic improvement in the agreement between the numerical (Euler) solution and the theory as $\epsilon$ is reduced from 0.38 to 0.2, with downstream flow rate fixed, especially as regards the position of wave crest B. What remain to be explained are (*a*) why the agreement does not improve further as $\epsilon$ is reduced to 0.1, (*b*) why the theory significantly overestimates the wavelength, and (*c*) why, when $\epsilon = 0.38$, the phase speed of the wave crests increases almost discontinuously (at $t \sim 0.4$) from the theoretical value to a roughly constant value about twice as great. The explanations could lie in physical effects, significant even when $\epsilon = 0.1$, that would be incorporated in the theory at higher order in $\epsilon$ but do not arise at the order taken in II; acceleration/deceleration of the mean flow when downstream flow rate is not fixed would come in this category. Alternatively, they could represent the fact that the theory is not strictly applicable to the problem in question, even at small $\epsilon$.

An explanation in the first category is the interaction of an eddy, or rather of a perturbation to the vorticity field, with its images in the channel walls. It is well known that a point vortex in an otherwise irrotational semi-infinite fluid moves parallel to a bounding plane wall, and a similar phenomenon is observed for 'fronts' of distributed vorticity (Stern & Pratt 1985). It is expected that the same effect will influence the present flows, although the fact that there are two walls gives rise to an infinite set of image vortices corresponding to each eddy. This effect does not arise in the theory of II, because it requires a perturbation to the vorticity, of $O(\epsilon)$ at most, to be advected by a perturbation to the velocity field which exists because of the zero-normal-velocity boundary condition on the channel wall. Such a velocity perturbation is no larger than $O(\epsilon^2)$ (the $O(\epsilon)$ perturbation satisfies the boundary condition – see II) so the relevant interaction will not arise before $O(\epsilon^3)$ in the vorticity transport equation, whereas the theory goes up only to $O(\epsilon^2)$. If, as it appears from figure 4, the vorticity in an eddy is greater than and of the same sign as the unperturbed vorticity at the same distance from the wall, and since the dominant interaction will be with the closest image in the wall, then this effect will result in an upstream shifting of the wave crests. Because eddy B is the strongest (with the possible exception of eddy A) the effect should be most marked for eddy B.

An explanation in the second category is related to the fact that the theory requires the flow to be slowly varying in the streamwise direction, i.e. the lengthscale of longitudinal variations, $\lambda a$, should be large compared with $a$: $\lambda = (10St)^{-\frac{1}{3}} = O(\epsilon^{-\frac{1}{2}})$. This is consistent with the observed and computed wave patterns some way downstream of the indentation, but not with the geometry of the indentation itself. Specifically, the dimensionless length over which the indentation height falls from $0.99\epsilon$ to $0.01\epsilon$ is between 1.1 and 1.2, which is not large compared with 1. The consequence will be an error in the theoretical flow pattern, and this error is likely to be most marked in the vicinity of the indentation, i.e. in the predicted form of eddy A. (It was noted in §5 that the main difference between cases with upstream and downstream flow rate fixed lay in the size of eddy A.) The theoretical results show the region occupied by eddy A to be shorter than eddy B, and the displacement of the core flow to be less above eddy A than above eddy B (this can be seen from figure 15 of II, which corresponds to a larger value of $St$, 0.057, than the flows computed here, but similar results were also obtained for $St = 0.037$). In our

but relative to a frame of reference accelerating and decelerating with the mean velocity. For the particular case analysed in this paper ($St = 0.037$) $l \approx 7.5\epsilon$, so even for $\epsilon = 0.1$ the importance of the acceleration term is confirmed.

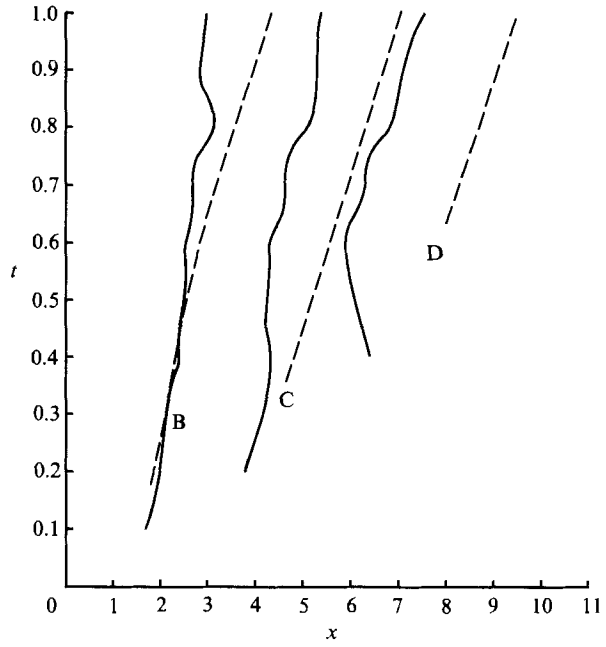


FIGURE 12. Positions of crests/troughs corresponding to eddies B, C and D as functions of time in inviscid flow, with $\epsilon = 0.38$, downstream flow rate fixed, modified according to the growth of eddy A (see text).

computations the reverse is true and the theory is not successful in predicting eddy A.

Thus, in assessing the equivalence of the theory and the Euler equation computations, we should adjust the positions of eddies B, C and D according to the growth of eddy A. Figure 11 shows the large-amplitude ($\epsilon = 0.38$) Euler solution (with downstream flow fixed) and small-amplitude theory to be in good agreement for eddy B for times up to about 0.4. If thereafter we subtract changes in the position of the reattachment point of eddy A from the positions of eddies B, C and D, the results are as shown in figure 12. Note that no adjustment to the theoretical predictions is made since the movement of 'eddy' A in the theory is small (II). The result is dramatic, in that the acceleration of eddies B, C and D, remarked on above, has been totally abolished, and indeed there seems to have been an over-correction since none of the eddies moves downstream as rapidly as in the theory. The mean phase velocity of wave B is slightly lower than that of C which is in turn lower than that of D. We attribute these reductions in phase velocity to the eddy–image interaction effect discussed above, which is expected to be weaker for the further downstream eddies.

The eddy–image interaction effect is also seen to have an influence on crest locations at smaller values of $\epsilon$, as seen in the $\epsilon = 0.1$ curves of figure 11, where it dominates the effect of the growth of eddy A. At intermediate values of $\epsilon$, the two effects may be almost balanced, as suggested by the excellent agreement with the theory for eddy B when $\epsilon = 0.2$ (figure 11).

It remains to seek an explanation for the wavelength in the numerical solution being significantly shorter than in the theory, even at small $\epsilon$. The only aspect of the theory which is obviously wrong at small $\epsilon$ is the slowly varying assumption ($\lambda \gg 1$),

with the consequence that eddy A grows more rapidly than predicted, at least later in the cycle and with downstream flow rate fixed. The wave front will continue to propagate downstream at roughly the mean fluid speed (see II), so if the same number of waves are generated between eddy A and the wave front, one would expect some reduction in wavelength when eddy A is growing faster. A more quantitative explanation is not available, however.

### 7.2. *Further discussion of the viscous flows*

Perhaps the most striking features of the viscous vis-à-vis the inviscid solutions, when downstream flow rate is fixed, are that (i) when $\epsilon = 0.38$ the crest positions agree closely until quite late in the cycle; thereafter the waves propagate more rapidly in the viscous fluid (figure 7); (ii) a reduction in amplitude has a negligible effect on crest positions in a viscous fluid, while its effect is significant in an inviscid fluid (§6 and figure 11). Observation (i) suggests not only that the wave generation and propagation processes well downstream of the indentation are the same in the two cases, but that the factors determining the length of eddy A as a function of time are also the same. The former is not unexpected, since the initial vorticity distribution is the same and is not modified in the viscous fluid by bulk flow accelerations (§5). The latter, however, is surprising because the mechanism by which eddy A is generated cannot be the same in the two fluids. The more rapid wave propagation towards the end of the cycle in a viscous fluid is presumably due to a reduction in the vortex–image interaction caused by vorticity diffusion in a viscous fluid.

In a viscous fluid at large Reynolds number an eddy such as eddy A is generally thought to be formed as a result of breakaway separation in an adverse pressure gradient, with subsequent ejection of some vorticity from close to the boundary into the flow further out, and formation of a vortex sheet at the edge of the eddy. This process is essentially the same in internal as in external flow (Smith 1979; Bertram & Pedley 1983). In steady flow the length of the separated eddy downstream of an indentation in a channel becomes proportional to the Reynolds number $Re$ as $Re$ is increased (Smith & Duck 1980). The shear layer becomes parallel to the boundary, and the flow in the eddy is very sluggish. One might interpret the flat top of the lengthening eddy A in the viscous streamline plot (figure 6) as evidence that most of eddy A tends to conform with the above (quasi-steady) picture, although the concentration of closed streamlines, and the slope of the separation streamline, at the downstream end of that eddy shows that the reattachment process is not quasi-steady.

This picture, however, does not take account of the fact that an 'eddy A' region of closed streamlines forms in an inviscid fluid and the mechanism of its formation must be associated with the deformation and rolling up of undisturbed vortex lines and cannot be related to the 'classical' breakaway separation. It would be of considerable interest to see a detailed model of unsteady separation in rotational flow, in which the competing effects of breakaway vorticity ejection and roll-up of background vorticity were analysed together. In our case, the fact that the lengths of eddy A and the positions of eddy B are the same in the viscous and the inviscid calculations, at the larger values of $\epsilon$, suggests that the behaviour near reattachment is dominated by unsteady vortex dynamics and not by viscous effects.

At smaller amplitudes, on the other hand, the inviscid eddy A becomes shorter, while the viscous one remains the same length, although the wave pattern becomes extremely weak with downstream flow rate fixed (§6). Two comments can be made

about this: (*a*) the no-slip condition inevitably has a more marked effect on the weak separated eddy of small thickness when $\epsilon$ is small than on the strong, thick eddy at larger $\epsilon$; and (*b*) the tendency of the disturbed vorticity distribution to roll up and form an inviscid eddy is clearly reduced as $\epsilon$ becomes small.

We return finally to the solutions that correspond to the experiments of I and II, for a viscous fluid with upstream flow rate fixed. We have seen that acceleration/deceleration of the downstream flow causes a marked increase in the strengths of the waves and eddies (figure 6 compared with figure 4 of III) but that it has little effect on their positions, until $t \approx 0.65$ (figure 7), which are virtually independent of $\epsilon$ at all times (figure 9), in marked contrast to the inviscid case (figure 10). Agreement between viscous and inviscid crest positions is poor, even early in the cycle, unlike the case of fixed downstream flow rate. As discussed in §5, the differences are attributable (*a*) to the fact that the no-slip condition causes fresh vorticity (of alternating sign through the cycle) to be generated at the walls as the bulk flow is accelerated or decelerated, changing the basic vorticity distribution on which the vorticity waves are formed, and (*b*) to the amplification of the vorticity (or Tollmien–Schlichting) wave in the decelerative phases of the flow. A further difference, related to (*a*), is that the vortex–image interaction will be more complex, on account of the large amount of negative vorticity generated under the strong positive recirculation regions at the downstream ends of the eddies (see III, figure 8), which would tend to reduce the upstream velocity induced by the images. Eddy A grows in length throughout the cycle, and much of it remains parallel sided (III, figure 4), indicating the possible importance of quasi-steady, viscous separation dynamics there. The fact that crest positions are independent of $\epsilon$ reinforces the view that the presence of viscosity is an important determinant of the structure of eddy A, although the fact that they are independent of *Re* (in the range studied in III) shows that the magnitude of the viscosity is unimportant.

The authors are grateful to J. W. Elliott and O. R. Tutty for valuable discussions, particularly regarding the numerical methods. We acknowledge, with thanks, the financial support of the SERC.

## Appendix. Numerical filtering and boundary conditions

In the vorticity transport equation for inviscid flow, the criterion for filtering in either direction can be illustrated as follows, with nodes identified as in figure 13(*a*). If $\zeta_A$, etc. denote the nodal values of $\zeta$ before filtering, and $\Delta\zeta_{AB}$ represents $(\zeta_B - \zeta_A)$ etc., then we filter at node $C$ only if

$$\Delta\zeta_{AB}\,\Delta\zeta_{BC} < 0, \tag{A 1}$$

$$\Delta\zeta_{BC}\,\Delta\zeta_{CD} < 0, \tag{A 2}$$

and

$$\Delta\zeta_{CD}\,\Delta\zeta_{DE} < 0. \tag{A 3}$$

If filtering is to be carried out at $C$, then new values of $\zeta$ at $B$, $C$ and $D$, $\bar{\zeta}_B$, $\bar{\zeta}_C$ and $\bar{\zeta}_D$, are determined by

$$\bar{\zeta}_B = \zeta_B + 0.1\Delta\zeta_{BC}, \tag{A 4}$$

$$\bar{\zeta}_C = \zeta_C + 0.1(\Delta\zeta_{CD} - \Delta\zeta_{BC}) \tag{A 5}$$

and

$$\bar{\zeta}_D = \zeta_D - 0.1\Delta\zeta_{CD}, \tag{A 6}$$

which represent a viscous-like correction. This is precisely the method of Myers *et al.*

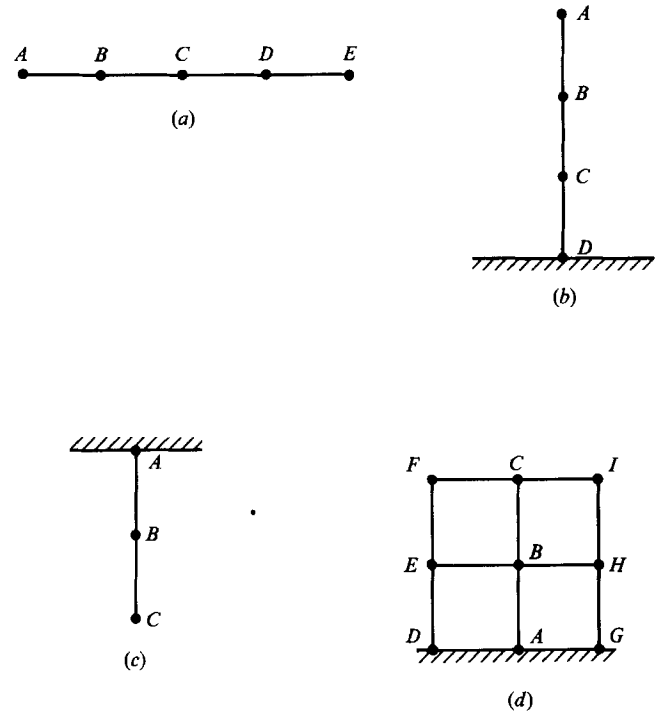


FIGURE 13. Nomenclature for nodes used in description of filtering and in expression for wall vorticity: (*a*) filtering at an internal point; (*b*) filtering near a wall; (*c*) vorticity at upper wall; (*d*) vorticity at lower wall.

(1981), but we have taken special action when filtering in the $y$-direction in the neighbourhood of a wall: a node at the wall was assumed not to satisfy the criterion for $y$-direction filtering, whilst an adjacent node was required to fulfil inequalities (A 1) and (A 2) only, with the notation of figure 13(*b*). Corrections were added according to (A 4)–(A 6). Finally, we note that no 'cosmetic' filtering of results was carried out.

The finite-difference expressions for the vorticity at the walls in inviscid flow are as follows, with nodes labelled as in figures 13(*c*) and 13(*d*), for the upper (unindented) and lower (indented) walls respectively. For the upper wall we have

$$\zeta_A = -p_{1A}^2 \frac{2\psi_B - \psi_A - \psi_C}{h^2}, \tag{A 7}$$

and for the lower wall

$$\zeta_A = -\frac{2\psi_A - \psi_D - \psi_G}{h^2} - 2p_{2A} \frac{-3\psi_G + 4\psi_H - \psi_I + 3\psi_D - 4\psi_E + \psi_F}{4h^2}$$
$$-(p_{1A}^2 + p_{2A}^2) \frac{2\psi_B - \psi_A - \psi_C}{h^2} - p_{3A} \frac{-3\psi_A + 4\psi_B - \psi_C}{2h}. \tag{A 8}$$

## REFERENCES

BERTRAM, C. D. & PEDLEY, T. J. 1983 Steady and unsteady separation in an approximately two-dimensional indented channel. *J. Fluid Mech.* **130**, 315–345.

GAD-EL-HAK, M., DAVIS, S. H., MCMURRAY, J. T. & ORSZAG, S. A. 1984 On the stability of the decelerating laminar boundary layer. *J. Fluid Mech.* **138**, 297–323.

HALL, P. & PARKER, K. H. 1976 The stability of the decaying flow in a suddenly blocked channel. *J. Fluid Mech.* **75**, 305–314.

MYERS, R. B., TAYLOR, T. D. & MURDOCK, J. J. 1981 Pseudo-spectral simulation of a two-dimensional vortex flow in a stratified, incompressible fluid. *J. Comput. Phys.* **43**, 180–188.

OBREMSKI, H. J., MORKOVIN, M. K. & LANDAHL, M. 1969 Portfolio of the stability characteristics of incompressible boundary layers. *AGARDograph* 134.

PEDLEY, T. J. & STEPHANOFF, K. D. 1985 Flow along a channel with a time-dependent indentation in one wall: the generation of vorticity waves. *J. Fluid Mech.* **160**, 337–367 (referred to as II).

RALPH, M. E. & PEDLEY, T. J. 1988 Flow in a channel with a moving indentation. *J. Fluid Mech.* **190**, 87–112 (referred to as III).

ROACHE, P. J. 1976 *Computational Fluid Dynamics*, 2nd edn. Hermosa.

SHAPIRO, M. A. & O'BRIEN, J. J. 1970 Boundary conditions for fine-mesh limited area forecasts. *J. Appl. Met.* **5**, 345–349.

SMITH, F. T. 1979 The separating flow through a severely constricted symmetric tube. *J. Fluid Mech.* **90**, 725–754.

SMITH, F. T. & DUCK, P. W. 1980 On the severe non-symmetric constriction, curving or cornering of channel flows. *J. Fluid Mech.* **90**, 727–753.

SOBEY, I. J. 1980 On flow through furrowed channels. Part 1. Calculated flow patterns. *J. Fluid Mech.* **96**, 1–26.

SOBEY, I. J. 1983 The occurrence of separation in oscillatory flow. *J. Fluid Mech.* **134**, 247–257.

STEPHANOFF, K. D., PEDLEY, T. J., LAWRENCE, C. J. & SECOMB, T. W. 1983 Fluid flow along a channel with an asymmetric oscillating constriction. *Nature* **305**, 692–695 (referred to as I).

STERN, M. E. & PRATT, L. J. 1985 Dynamics of vorticity fronts. *J. Fluid Mech.* **161**, 513–532.